# Stellar $(n, \gamma)$ cross sections for Br and Rb: Matching the weak and main *s*-process components

M. Heil,* F. Käppeler, and E. Uberseder†
*Forschungszentrum Karlsruhe, Institut für Kernphysik, Postfach 3640, D-76021 Karlsruhe, Germany*

R. Gallino,‡ S. Bisterzo, and M. Pignatari§
*Dipartimento di Fisica Generale, Università di Torino, via P. Giuria 1, I-10125 Torino, Italy*
(Received 11 February 2008; revised manuscript received 29 April 2008; published 8 August 2008)

The stellar $(n, \gamma)$ cross sections of $^{79}$Br, $^{81}$Br, $^{85}$Rb, and $^{87}$Rb have been determined by a series of ten activation measurements in a quasistellar neutron spectrum corresponding to a thermal energy of $kT = 25$ keV. The final uncertainties between 3 and 10% were dominated by the $\gamma$-ray intensities in the decay of the respective reaction products. All other uncertainties were significantly reduced through variation of the experimental parameters. The consequences of these results for *s*-process nucleosynthesis of Br and Rb, and in particular of the local *s*-only isotopes $^{80,82}$Kr and $^{86,87}$Sr, are discussed with respect to the branching points at $^{79}$Se and $^{85}$Kr. The contributions of both the main *s* component from thermally pulsing low mass asymptotic giant branch stars and the weak *s* component from massive stars are considered in this analysis.

DOI: 10.1103/PhysRevC.78.025802 PACS number(s): 25.40.Lw, 26.20.−f, 27.40.+z, 27.50.+e

## I. INTRODUCTION

The *s*-process components of the solar abundances in the Br-Kr-Rb-Sr region are characterized by the superposition of abundance contributions from the main *s* process associated with thermally pulsing low mass asymptotic giant branch (AGB) stars and from the weak *s* process during core He and shell C burning in massive stars. However, the two components contribute in completely different ways. While the relative strength of the weak component decreases significantly with mass number, that of the main component is rapidly growing. The complexity of this situation is further enhanced if one recalls that the weak and the main *s* process exhibit two very different neutron capture regimes. For this reason, the branchings at $^{79}$Se and $^{85}$Kr, which are sketched in Fig. 1, represent the most problematic part of the entire *s*-process path.

In massive stars, the *s* process occurs first during convective core He burning and subsequently during convective carbon shell burning. Neutrons are produced by the $^{22}$Ne$(\alpha, n)^{25}$Mg reaction in both cases, but at rather different temperatures and neutron densities. Because of the lower temperatures in the core He burning, $^{22}$Ne$(\alpha, n)^{25}$Mg is only activated close to the He exhaustion in the last $\sim 10^4$ yr, when $T_8 \sim 0.3$ (units of $10^8$ K), providing neutron densities on the order of $\leqslant 10^6$ cm$^{-3}$. In the following convective C shell phase the temperature is about $T_9 \sim 1$ (units of $10^9$ K), and neutrons can be produced for $\sim$1 yr. Under these conditions, the neutron density regime is orders of magnitude higher than that in the He core, reaching peak values of $10^{11}$–$10^{12}$ cm$^{-3}$ [1,2]. The neutron exposures (or time-integrated neutron fluxes) in the He core and in the C shell are affected by the stellar mass and metallicity, but also by the cross section of the $^{22}$Ne$(\alpha, n)^{25}$Mg reaction. It was found that reaction flow equilibrium could not be reached in massive stars because of the unfavorable neutron/seed ratio. Therefore, single cross sections can have a significant impact on the reaction flow, thus affecting the *s* abundances over a sequence of subsequent isotopes. For example, this propagation effect has been discussed for $^{62}$Ni [3,4].

In thermally pulsing low mass AGB stars one finds that most of the neutron exposure is provided during the radiative interpulse phase of shell hydrogen burning via $^{13}$C$(\alpha, n)^{16}$O reactions in the so-called $^{13}$C pocket [5]. In this situation the neutron density is limited to about $10^7$ cm$^{-3}$ because of the comparably low temperature of $T_8 = 1$. Although the neutron exposure in the subsequent He shell flashes is 20 times smaller, the higher temperature of $T_8 = 3$ leads to neutron bursts with densities of up to $10^{10}$ cm$^{-3}$ [6].

The different temperature and neutron density regimes described above have a strong impact on the abundance pattern of *s*-process branchings through the competition between $(n, \gamma)$ reactions, which depend on neutron density, and $\beta$ decays, which—in some cases—depend on temperature as well [7]. The relative contributions of the two *s* components reported in previous studies [2,8,9] exhibit significant discrepancies as illustrated in Table I and need to be updated with meanwhile improved models for stellar He burning and Galactic chemical evolution (GCE).

Quantitative investigations of these aspects have to rely on accurate stellar $(n, \gamma)$ cross sections. Existing data for $^{85}$Rb and $^{87}$Rb suffer from unacceptably large discrepancies and from considerable uncertainties [10]. Two measurements were performed on $^{85}$Rb so far, one with the time of flight (TOF) technique [11] and one by activation [12]. The stellar cross sections obtained in these measurements differ by 50%. Similarly, data for $^{87}$Rb exhibit differences of 25% although

*Present address: GSI Darmstadt, Planckstr. 1, 64291 Darmstadt, Germany; M.Heil@gsi.de
†Present address: University of Notre Dame, Notre Dame, USA.
‡Second address: Center for Stellar, Planetary Astrophysics, School of Mathematical Sciences, Monash University, PO Box 28, Victoria 3800, Australia.
§Present address: Keele University, Keele, Staffordshire ST5 5BG, UK.

 

TABLE I. Abundance components[a] due to the weak and main *s* processes from previous studies.

| Isotope | Low mass stars[b] | | Massive stars | | Total | | |
|---|---|---|---|---|---|---|---|
| | (1993)[c] | (1999)[d] | Core He | Shell C | (1993)[c] | (1999)[d] | (2004)[e] |
| $^{78}$Se | 0.22 | 0.11 | 0.09 | 0.28 | 0.59 | 0.48 | |
| $^{80}$Se | 0.18 | 0.09 | 0.00 | 0.15 | 0.33 | 0.24 | |
| $^{79}$Br | 0.18 | 0.09 | 0.03 | 0.26 | 0.47 | 0.38 | |
| $^{81}$Br | 0.17 | 0.09 | 0.03 | 0.16 | 0.36 | 0.28 | |
| $^{80}$Kr | 0.16 | 0.12 | 0.43 | 0.43 | 1.02 | 0.98 | |
| $^{82}$Kr | 0.67 | 0.37 | 0.19 | 0.34 | 1.20 | 0.90 | |
| $^{83}$Kr | 0.20 | 0.13 | 0.06 | 0.13 | 0.39 | 0.32 | |
| $^{84}$Kr | 0.23 | 0.14 | 0.04 | 0.10 | 0.37 | 0.28 | |
| $^{86}$Kr | 1.11 | 0.27 | 0.00 | 0.13 | 1.24 | 0.40 | |
| $^{85}$Rb | 0.24 | 0.16 | 0.03 | 0.16 | 0.43 | 0.35 | |
| $^{87}$Rb | 1.05 | 0.35 | 0.00 | 0.14 | 1.19 | 0.49 | |
| $^{86}$Sr | 0.92 | 0.47 | 0.14 | 0.10 | 1.16 | 0.71 | 0.76 |
| $^{87}$Sr | 0.78 | 0.50 | 0.12 | 0.04 | 0.94 | 0.76 | 0.70 |
| $^{88}$Sr | 0.83 | 0.92 | 0.03 | 0.04 | 0.90 | 0.99 | 0.82 |

[a]Fractions of solar abundances [48].
[b]AGB models with masses from 1.5 to 3 $M_\odot$.
[c]Reference [2].
[d]Reference [8].
[e]Average over GCE including IMS [9].

uncertainties between 3 and 10% have been claimed [10]. More recently, this cross section has been studied by two TOF experiments [11,13] and by one activation [2]. In this context, it is important to note that the cross section of $^{86}$Rb, which determines the role of this isotope as an additional branch point, is still estimated to be uncertain by almost a factor of two [10].

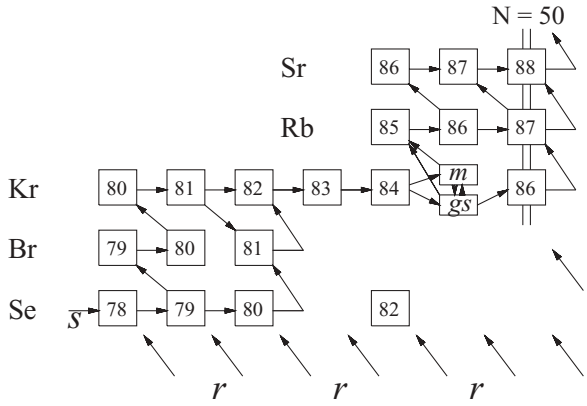


FIG. 1. The *s*-process branchings at $^{79}$Se and $^{85}$Kr are important because of the pronounced temperature dependence of the respective half-lives. Minor branchings with a strength of less than 5% have been omitted in the plot but are considered in the calculations. While the $^{79}$Se decay is known to be drastically enhanced due to thermal population of the 3.9 min isomer [28], the case of $^{85}$Kr depends on the theoretical description of thermal equilibration [7]. In massive stars significant branchings are obtained only during shell C burning, before the main reaction flow is almost unbranched because of the much lower neutron densities during core-He burning. The situation in low mass stars is more complex, because the half-life of $^{79}$Se is practically not affected during the low-temperature phase when the *s* process operates in the $^{13}$C pocket. Accordingly the branch to $^{80}$Kr opens only later at the higher temperatures reached in He shell flashes.

As far as the available data for $^{79}$Br and $^{81}$Br are concerned, the situation resembles that of the Rb cross sections. Apart from older uncertain measurements, a TOF experiment [14] and a work based on the activation technique [15] differed by 15 and 30%, although uncertainties between 4 and 6% had been claimed by the authors.

In an effort to resolve the discrepancies and to improve the accuracy of the stellar cross sections for the stable Br and Rb isotopes, a series of activation measurements was performed. In fact, systematic uncertainties were significantly reduced by variation of the experimental parameters. Measurements and data analysis are described in Secs. II and III, the results are presented in Sec. IV, and the astrophysical implications are discussed in Sec. V.

## II. MEASUREMENTS

### A. Experimental technique

The activation method represents a well-established and accurate approach to determine Maxwellian averaged cross sections (MACS) at $kT = 25$ keV. This method, which is based on a quasistellar neutron spectrum produced by means of the $^7$Li$(p, n)^7$Be reaction [16,17], has been extensively used for *s*-process studies (for recent examples, see Refs. [18–20]).

In the measurements reported here, proton beams of typically 100 $\mu$A from the Karlsruhe 3.7 MV Van de Graaff accelerator were used for neutron production. The quasistellar spectra were obtained by bombarding 30-$\mu$m-thick metallic Li layers evaporated onto a water cooled copper backing with a beam energy of $E_p = 1912$ keV, 30 keV above the reaction threshold. In this way, neutrons are kinematically collimated into a forward cone of 120° opening angle. Neutron

TABLE II. Samples and irradiation parameters.

| Activation | Sample | Mass (mg) | Diameter (mm) | Irradiation time (min) | Integrated flux ($\times 10^{13}$) |
|---|---|---|---|---|---|
| 1 | RbBr | 72.58 | 6 | 249 | 4.41 |
| 2 | RbBr | 349.60 | 10 | 37 | 0.606 |
| 3 | RbBr | 692.12 | 12 | 10 | 0.0990 |
| 4 | KBr | 98.70 | 6 | 156 | 2.68 |
| 5 | KBr | 733.27 | 12 | 1118 | 7.07 |
| 6 | RbNO3 | 406.00 | 10 | 49 | 0.658 |
| 7 | RbCl | 96.55 | 6 | 2447 | 25.6 |
| 8 | RbCl | 225.83 | 10 | 1094 | 6.36 |
| 9 | RbNO3 | 95.92 | 6 | 1755 | 35.9 |
| 10 | RbNO3 | 186.26 | 10 | 1135 | 8.86 |

moderation is avoided because cooling is achieved by lateral heat conduction to the water flow outside of this cone. Throughout the irradiations the neutron flux is continuously monitored and recorded in time steps of typically 60 s by means of a $^{6}$Li-glass detector at 1 m distance from the target. This information is important to account for fluctuations of the neutron yield in evaluating the fraction $f_b$ of the reaction products that decay already during the irradiations.

A comparison of the resulting quasistellar neutron spectrum with a true Maxwell-Boltzmann distribution is given in Fig. 2.

### B. Samples and irradiations

The samples were pellets pressed from various Rb and Br compounds of natural composition. As listed in Table II repeated activations were performed with samples, which differed in diameter between 6 and 12 mm and in thickness between 0.8 and 2.5 mm. The samples were sandwiched between 0.03-mm-thick gold foils for normalization to the well-known gold reference cross section [17] and were placed completely inside the neutron cone, in direct contact with the neutron target at the position of highest flux.

Depending on the half-lives of the respective product nuclei, the irradiations lasted between 40 h in the case of $^{87}$Rb and 10 min for measuring the partial cross section to the ground state of $^{80}$Br. The integrated neutron flux seen by the samples

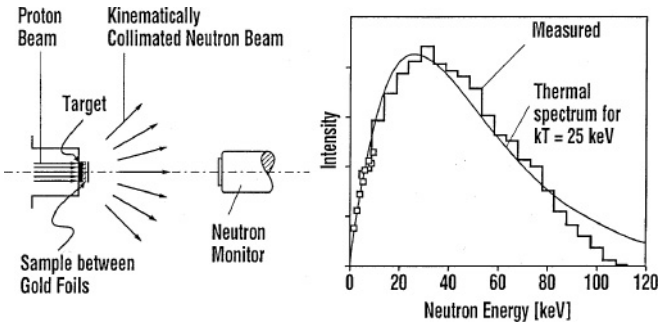


FIG. 2. (Left) Schematic sketch of the activation setup. (Right) The quasistellar neutron spectrum obtained with the $^{7}$Li$(n, \gamma)^{7}$Be reaction (histogram and symbols) compared to a true Maxwell-Boltzmann distribution for a thermal energy of $kT = 25$ keV. Note that the thermal spectrum is truncated at 106 keV.

(last column of Table II) reflects the condition of the accelerator and the performance of the $^{7}$Li targets used and corresponds to an average source strength of about $2 \times 10^{9}$ s$^{-1}$. In total, ten activations were carried out for the determination of the three $(n, \gamma)$ cross sections of $^{81}$Br, $^{85}$Rb, and $^{87}$Rb and of the partial cross sections to ground state and isomer in $^{80}$Br.

### C. Induced activities

The induced activities are characterized by energetic $\gamma$-ray lines. Except for the decay of $^{80}$Br, the relative intensities of these transitions were well known (Table III).

The $\gamma$ activities were counted by means of a shielded 76 cm$^3$ high purity Ge detector (HPGe) with 1.7 keV resolution at 1.33 MeV $\gamma$-ray energy and a relative efficiency of 30%. The counting geometry was exactly defined by a special adapter for the reproducible positioning of the samples within 0.1 mm. The corresponding uncertainty for the efficiency of the detector was calculated to be less than 0.3%, negligible compared to other contributions. In the relevant energy range between 412 and 1317 keV the photo peak detection efficiencies were determined to an accuracy of $\pm 1.5\%$ by a set of calibrated sources.

In all cases $\gamma$-ray backgrounds were small and had practically no effect on the uncertainty of the final cross section values. The excellent sensitivity of the experimental method is illustrated in Fig. 3 in the example of the $^{85}$Rb$(n, \gamma)^{86}$Rb reaction. Despite the fact that the induced activities were low because of the long half-life of $^{86}$Rb, the statistical uncertainties were much smaller than the respective systematic uncertainties (see below).

## III. DATA ANALYSIS

The total number of activated nuclei $A$ after the irradiation time $t_i$ is given by

$$A(t_i) = \Phi_T \cdot N \cdot \sigma \cdot f_b, \tag{1}$$

where $\Phi_T$ is the time-integrated neutron flux, $N$ the number of sample atoms per cm$^2$, and $\sigma$ the spectrum averaged neutron capture cross section. The factor $f_b$ accounts for variations of the neutron flux and for the decay during activation.

TABLE III. Decay properties of the product nuclei.

| Product nucleus | Half-life | $\gamma$-ray energy (keV) | Intensity per decay (%) | Reference |
|---|---|---|---|---|
| $^{80}$Br(g) | $17.68 \pm 0.02$ min | 616.3 | $6.7 \pm 0.6$ | [23] |
| | | 665.8 | $1.08 \pm 0.13$ | |
| $^{82}$Br | $35.282 \pm 0.007$ h | 554.35 | $62.45 \pm 0.85$ | [49] |
| | | 698.37 | $28.273 \pm 0.43$ | |
| | | 776.52 | $83.4 \pm 1.2$ | |
| | | 1044.00 | $28.273 \pm 0.43$ | |
| | | 1317.47 | $26.771 \pm 0.41$ | |
| $^{86}$Rb | $18.642 \pm 0.018$d | 1077.0 | $8.64 \pm 0.04$ | [50] |
| $^{88}$Rb | $17.773 \pm 0.011$ min | 898.03 | $14.68 \pm 0.13$ | [51] |
| $^{198}$Au | $2.69517 \pm 0.00021$d | 411.8 | $95.58 \pm 0.12$ | [52] |

The cross section can then be calculated from the number of counts in a characteristic $\gamma$-ray line,

$$C_\gamma = A \cdot K_\gamma \cdot \varepsilon_\gamma \cdot I_\gamma \cdot [1 - \exp(-\lambda t_m)] \cdot \exp(-\lambda t_w), \qquad (2)$$

where $K_\gamma$ is a correction factor for $\gamma$-ray self-absorption, $\varepsilon_\gamma$ the efficiency of the HPGe detector, $I_\gamma$ the line intensity, $t_w$ the waiting time between irradiation and counting, and $t_m$ the duration of the activity measurement. The time-integrated flux, $\Phi$, is determined from the measured intensities of the 412 keV $\gamma$-ray line in the spectra of the two gold foils. This analysis was applied for the isotopes $^{81}$Br, $^{85}$Rb, and $^{87}$Rb. For $^{79}$Br one must consider that neutron capture can lead to the ground state of $^{80}$Br with a half-life of 17.68 min or to an isomeric state with a half-life of 4.4205 h which then feeds the ground state by internal transition or conversion electrons during the activation runs. Because the $\gamma$ rays from this decay had an energy of 37 keV only, the cross section to the isomeric state was measured also via the decay of the ground state. In this case the total number of activated nuclei after the irradiation is

$$A_m(t_i) = \Phi_T \cdot N \cdot \sigma_m \cdot f_b^m \qquad (3)$$

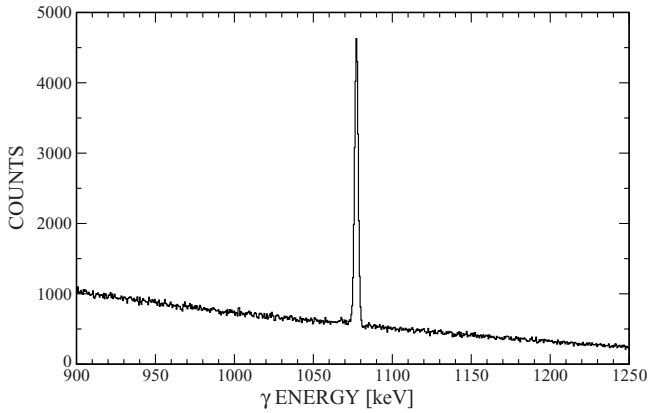


FIG. 3. The $\gamma$-ray spectrum after activation 8 corresponds to the most unfavorable case of the $^{85}$Rb$(n,\gamma)^{86}$Rb reaction, where the produced activity is comparably low because of the long half-life of $^{86}$Rb. Nevertheless, the counting statistics of the line at 1077 keV are much better than the systematic uncertainties discussed in Sec. III.

for the isomeric state and

$$A_g(t_i) = \Phi_T \cdot N \cdot (\sigma_g \cdot f_b^g + \sigma_m \cdot \lambda_m \cdot g_m) \qquad (4)$$

for the ground state, with

$$g_m = \left\{ \int_0^{t_i} \int_0^{t} \exp[\lambda_g (t - t_i)] \cdot \exp[\lambda_m (t' - t)] \cdot \Phi(t') dt' dt \right\} \Big/ \int_0^{t_i} \Phi(t) dt. \qquad (5)$$

The number of counts in the characteristic $\gamma$-ray peak can then be described by

$$C_\gamma = K_\gamma \cdot \varepsilon_\gamma \cdot I_\gamma \cdot \left\{ A_g(t_i) \cdot \exp(-\lambda_g t_w) \cdot (1 - \exp(-\lambda_g t_c)) + A_m(t_i) \cdot \left[ \frac{\lambda_m}{\lambda_g - \lambda_m} \cdot \exp(-\lambda_m t_w) \cdot (1 - \exp(-\lambda_m t_c)) - \frac{\lambda_m}{\lambda_g - \lambda_m} \cdot \exp(-\lambda_g t_w) \cdot (1 - \exp(-\lambda_g t_c)) \right] \right\}.$$

In the analysis, the number of activated nuclei after the activation for the ground and isomeric state ($A_g$ and $A_m$) was obtained by fitting the above formula to the decay curve (Fig. 4). The cross sections $\sigma_m$ and $\sigma_g$ were then obtained from Eqs. (3) and (4).

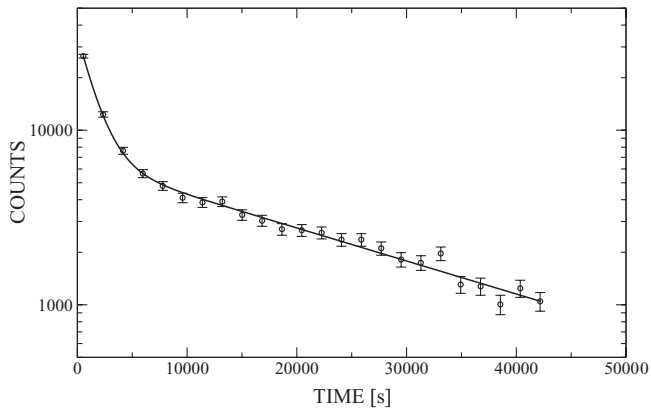


FIG. 4. Decay curve of $^{80}$Br$^{g}$ deduced from the intensity of the 616.3 keV $\gamma$-ray transition (data from activation 4).

TABLE IV. Compilation of systematic uncertainties.

| Source of uncertainty | Uncertainty (%) | | | | | |
|---|---|---|---|---|---|---|
| | Au | $^{79}$Br(g) | $^{79}$Br(m) | $^{81}$Br | $^{85}$Rb | $^{87}$Rb |
| Gold cross section | 1.5 | – | – | – | – | – |
| Number of nuclei | 0.6 | 0.3 | 0.3 | 0.1 | 0.1 | 0.03 |
| Time factors, $f_w$, $f_m$, $f_b$, and $\tau_{1/2}$ | | | $\leqslant 0.1$ | | | |
| Self-absorption | | | $\leqslant 1.0$ | | | |
| Detector efficiency | | | $\leqslant 1.5$ | | | |
| $\gamma$-ray intensity per decay | 0.13 | 9.0 | 9.0 | 1.5 | 0.5 | 0.9 |
| Neutron flux | – | 2.6 | 2.6 | 2.4 | 2.4 | 2.5 |
| Fitting procedure | – | 1.0 | 2.0 | – | – | – |
| Total uncertainty of cross section | – | 9.6 | 9.8 | 3.7 | 3.0 | 3.2 |

The experimental uncertainties are summarized in Table IV, where the investigated reactions are indicated by the respective target nuclei.

Significant contributions to the overall uncertainty originate from the gold reference cross section, the efficiency of the HPGe detectors, and the time-integrated neutron flux. The latter contribution is mainly due to the effect of the divergent neutron intensity, which was corrected on the basis of experimental data measured with a stack of gold foils [21]. The partial $^{79}$Br cross sections are also affected by the uncertain $\gamma$-decay intensity of $^{80}$Br.

Because the statistical uncertainties from the activity measurements became practically negligible after combining the results from repeated activations, the final uncertainties are determined by systematic effects and are, therefore, comparable to those of the individual activations.

## IV. RESULTS AND MAXWELLIAN AVERAGES

Table V shows a summary of the results obtained in all ten activations together with the corresponding uncertainties. In all cases, the differences among these results are well within the estimated uncertainties, thus confirming the procedures applied in data analysis.

The cross sections in the last two columns of Table V represent averaged cross sections for the quasistellar neutron

TABLE V. Activations, $\gamma$ counting, and cross section results.[a]

| Reaction | Activation | $\gamma$-ray energy (keV) | Self-absorption correction | Cross section[b] (mb) | Mean value (mb) |
|---|---|---|---|---|---|
| $^{79}$Br$(n,\gamma)^{80}$Br$^{g}$ | 3 | 616.3 | 0.97 | $476 \pm 3 \pm 45$ | |
| $^{79}$Br$(n,\gamma)^{80}$Br$^{g}$ | 4 | 616.3 | 0.97 | $445 \pm 3 \pm 41$ | |
| $^{79}$Br$(n,\gamma)^{80}$Br$^{g}$ | 4 | 665.8 | 0.99 | $468 \pm 6 \pm 56$ | $460 \pm 44$ |
| $^{79}$Br$(n,\gamma)^{80}$Br$^{m}$ | 3 | 616.3 | 0.97 | $169 \pm 4 \pm 16$ | |
| $^{79}$Br$(n,\gamma)^{80}$Br$^{m}$ | 4 | 616.3 | 0.97 | $171 \pm 2 \pm 16$ | |
| $^{79}$Br$(n,\gamma)^{80}$Br$^{m}$ | 4 | 665.8 | 0.99 | $185 \pm 2 \pm 22$ | $174 \pm 17$ |
| $^{81}$Br$(n,\gamma)^{82}$Br | 4 | 554.35 | 0.99 | $242 \pm 2 \pm 9$ | |
| $^{81}$Br$(n,\gamma)^{82}$Br | 4 | 776.52 | 0.99 | $236 \pm 3 \pm 9$ | |
| $^{81}$Br$(n,\gamma)^{82}$Br | 1 | 554.35 | 0.99 | $254 \pm 1 \pm 9$ | |
| $^{81}$Br$(n,\gamma)^{82}$Br | 5 | 554.35 | 0.98 | $244 \pm 1 \pm 9$ | |
| $^{81}$Br$(n,\gamma)^{82}$Br | 5 | 776.52 | 0.98 | $246 \pm 1 \pm 9$ | |
| $^{81}$Br$(n,\gamma)^{82}$Br | 3 | 554.35 | 0.97 | $243 \pm 2 \pm 9$ | |
| $^{81}$Br$(n,\gamma)^{82}$Br | 3 | 698.37 | 0.97 | $248 \pm 4 \pm 9$ | |
| $^{81}$Br$(n,\gamma)^{82}$Br | 3 | 776.52 | 0.97 | $243 \pm 2 \pm 9$ | |
| $^{81}$Br$(n,\gamma)^{82}$Br | 3 | 1044.00 | 0.98 | $245 \pm 5 \pm 9$ | |
| $^{81}$Br$(n,\gamma)^{82}$Br | 3 | 1317.47 | 0.98 | $252 \pm 5 \pm 9$ | $245 \pm 9$ |
| $^{85}$Rb$(n,\gamma)^{86}$Rb | 7 | 1077.0 | 0.99 | $232 \pm 2 \pm 7$ | |
| $^{85}$Rb$(n,\gamma)^{86}$Rb | 8 | 1077.0 | 0.99 | $237 \pm 6 \pm 7$ | |
| $^{85}$Rb$(n,\gamma)^{86}$Rb | 9 | 1077.0 | 0.99 | $234 \pm 2 \pm 7$ | |
| $^{85}$Rb$(n,\gamma)^{86}$Rb | 10 | 1077.0 | 0.99 | $236 \pm 2 \pm 7$ | $235 \pm 7$ |
| $^{87}$Rb$(n,\gamma)^{88}$Rb | 2 | 898.03 | 0.98 | $13.1 \pm 1.1 \pm 0.4$ | |
| $^{87}$Rb$(n,\gamma)^{88}$Rb | 3 | 898.03 | 0.98 | $16.5 \pm 3.0 \pm 0.5$ | |
| $^{87}$Rb$(n,\gamma)^{88}$Rb | 6 | 898.03 | 0.98 | $13.8 \pm 0.4 \pm 0.5$ | $13.9 \pm 0.6$ |

[a]Cross section averaged over quasi-stellar spectrum.
[b]Statistical and systematic uncertainties listed separately.

TABLE VI. Normalization factors $NF$ for the differential cross sections from evaluated data libraries.

| Library | Normalization factors $NF$ | | | |
|---|---|---|---|---|
| | $^{79}$Br | $^{81}$Br | $^{85}$Rb | $^{87}$Rb |
| JEFF/3.1 | 0.85 | 0.53 | 0.87 | 0.76 |
| JENDL/3.3 | 0.90 | 0.94 | 0.79 | 0.66 |
| ENDF/VI-8 | 0.85 | 0.53 | 1.05 | 0.99 |

distribution. Though this experimental spectrum represents a very good approximation of the thermal situation for $kT = 25$ keV, the cutoff at 106 keV requires a small correction. In the present case the difference between a true Maxwell-Boltzmann shape and the neutron spectrum used resulted in corrections between $-7\%$ and $+7\%$. This problem of the cross section shape affects also the extrapolation of the measured 25 keV values to $kT = 30$ keV, which is commonly used for the comparison of $s$-process data, as well as to other thermal energies typical for the various $s$-process scenarios.

For the calculation of the final MACSs,

$$\langle\sigma\rangle_{kT} = \frac{\langle\sigma v\rangle}{v_T} = \frac{2}{\sqrt{\pi}} \frac{\int_0^\infty \sigma(E_n)\cdot E_n \cdot \exp(-E_n/kT)\cdot dE_n}{\int_0^\infty E_n \cdot \exp(-E_n/kT)\cdot dE_n}; \quad (6)$$

this correction was obtained by normalizing the corresponding differential $(n,\gamma)$ cross sections of the isotopes under investigation, $\sigma_{n,\gamma}(E_n)$, to the new experimental values.

Differential cross sections are available online from various data libraries, e.g., JEFF/3.1 (www.nea.fr/html/dbdata/JEFF/), JENDL/3.3 (wwwndc.tokai-sc.jaea.go.jp/jendl/), and ENDF/B-VI.8 (www.nndc.bnl.gov/). In a first step, these cross sections were folded with the experimental spectrum—instead of the Maxwell-Boltzmann distribution in Eq. (6)—for direct comparison with the measured values. The corresponding ratios $NF = \sigma_{\rm exp}/\sigma_{\rm lib}$ listed in Table VI represent the normalization factors that must be applied to the evaluated data if these are to be used for extrapolation to lower and higher thermal energies (see below).

If the normalization factor $2/\sqrt{\pi}$ [Eq.(6)] is taken into account, the MACSs at $kT = 25$ keV calculated with the normalized evaluated data are in good agreement with the measured cross sections (Table V). This confirms that the experimental neutron spectrum is a very good approximation of the true thermal distribution. Nevertheless, there are nonnegligible differences, which reflect differences in the energy dependence of the evaluated cross sections. The MACSs obtained in this way are summarized in Table VII for comparison with the compilation of Bao *et al.* [10].

The recommended values in Table VII are based on the energy dependence adopted in the compilation of Bao *et al.* [10]. The quoted uncertainties are composed of the

TABLE VII. Recommended MACSs of $^{79}$Br, $^{81}$Br, $^{85}$Rb, and $^{87}$Rb compared to existing evaluations and to the compilation of Bao *et al.* [10].

| $kT$ (keV) | MACS (mb) | | | | | | | | | | |
|---|---|---|---|---|---|---|---|---|---|---|---|
| | 5 | 10 | 15 | 20 | 25 | 30 | 40 | 50 | 60 | 80 | 100 |
| | | | | | | $^{79}$Br$(n,\gamma)^{80}$Br | | | | | |
| Ref. [10] | 1767 | 1177 | 932 | 791 | 696 | 627 | 532 | 468 | 435 | 370 | 305 |
| Ref. [10][a] | $1726^{+165}_{-166}$ | $1152^{+110}_{-117}$ | $912^{+87}_{-90}$ | $774^{+74}_{-75}$ | 681±65 | $613^{+59}_{-59}$ | $521^{+53}_{-50}$ | $458^{+48}_{-44}$ | $426^{+42}_{-41}$ | $362^{+36}_{-36}$ | $298^{+40}_{-28}$ |
| JEFF | 1722 | 1130 | 898 | 769 | 683 | 622 | 537 | 479 | 436 | 372 | 326 |
| JENDL | 1709 | 1113 | 889 | 763 | 678 | 615 | 527 | 466 | 420 | 352 | 304 |
| ENDF | 1716 | 1127 | 896 | 767 | 682 | 621 | 537 | 479 | 435 | 371 | 325 |
| | | | | | | $^{81}$Br$(n,\gamma)^{82}$Br | | | | | |
| Ref. [10] | 960 | 614 | 478 | 402 | 350 | 313 | 264 | 232 | 217 | 187 | 157 |
| Ref. [10][a] | $720^{+27}_{-111}$ | $460^{+18}_{-37}$ | $358^{+14}_{-19}$ | $301^{+11}_{-13}$ | 262±10 | $235^{+9}_{-9}$ | $198^{+10}_{-9}$ | $174^{+10}_{-9}$ | $163^{+6}_{-14}$ | $140^{+5}_{-15}$ | $118^{+7}_{-9}$ |
| JEFF | 612 | 427 | 345 | 296 | 263 | 238 | 204 | 181 | 164 | 140 | 123 |
| JENDL | 710 | 462 | 359 | 300 | 260 | 232 | 193 | 168 | 150 | 126 | 110 |
| ENDF | 622 | 432 | 348 | 298 | 264 | 239 | 204 | 181 | 164 | 140 | 123 |
| | | | | | | $^{85}$Rb$(n,\gamma)^{86}$Rb | | | | | |
| Ref. [10] | 724 | 482 | 375 | 313 | 271 | 240 | 199 | 172 | 153 | 129 | 110 |
| Ref. [10][a] | $666^{+19}_{-224}$ | $443^{+12}_{-129}$ | $345^{+10}_{-60}$ | $288^{+8}_{-24}$ | 249±7 | $221^{+13}_{-6}$ | $183^{+24}_{-5}$ | $158^{+28}_{-4}$ | $141^{+29}_{-4}$ | $119^{+28}_{-3}$ | $101^{+28}_{-3}$ |
| JEFF | 505 | 387 | 325 | 282 | 251 | 228 | 193 | 170 | 152 | 128 | 111 |
| JENDL | 620 | 424 | 338 | 285 | 249 | 223 | 186 | 161 | 143 | 118 | 103 |
| ENDF | 443 | 315 | 286 | 265 | 248 | 232 | 206 | 186 | 170 | 146 | 129 |
| | | | | | | $^{87}$Rb$(n,\gamma)^{88}$Rb | | | | | |
| Ref. [10] | 35.3 | 24.4 | 20.6 | 18.4 | 16.4 | 15.5 | 13.8 | 12.5 | 11.7 | 10.6 | 9.8 |
| Ref. [10][a] | $36.0^{+2.2}_{-5.6}$ | $24.9^{+3.9}_{-0.9}$ | $21.0^{+2.5}_{-0.8}$ | $18.8^{+1.5}_{-0.7}$ | 16.7±0.7 | $15.8^{+0.7}_{-0.9}$ | $14.1^{+0.6}_{-1.6}$ | $12.8^{+0.6}_{-2.1}$ | $11.9^{+0.5}_{-2.3}$ | $10.8^{+0.5}_{-2.3}$ | $10.0^{+0.4}_{-2.3}$ |
| JEFF | 28.9 | 22.8 | 20.3 | 18.3 | 16.7 | 15.3 | 13.4 | 11.9 | 10.9 | 9.3 | 8.3 |
| JENDL | 31.5 | 25.0 | 21.4 | 18.8 | 16.8 | 15.3 | 13.1 | 11.6 | 10.5 | 9.0 | 8.0 |
| ENDF | 34.3 | 21.1 | 18.6 | 17.5 | 16.7 | 15.9 | 14.6 | 13.6 | 12.7 | 11.3 | 10.3 |

[a]Ref. [10] normalized to new values.

experimental contribution and an additional component due to the extrapolation to lower and higher thermal energies. The latter part was estimated by comparison with the respective values in lines 3 to 5 of Table VII.

In all cases, stellar enhancement factors (SEF) are negligible up to thermal energies of 40 keV and are smaller than 10% at 100 keV [10,22].

### A. $^{79}$Br$(n, \gamma)^{80}$Br cross section

Neutron capture on $^{79}$Br feeds the short-lived ground state ($t_{1/2} = 17.68$ min) as well as the 4.42 h isomeric state. Because the 37 keV internal transition could not be detected without large absorption corrections, this component was derived from the time behavior of the ground state decay as described in Sec. III. The comparably large uncertainties for the two partial $(n, \gamma)$ cross sections are due to the poorly known decay intensities [23].

Compared to a previous activation measurement [24], the present isomeric ratio, IR $= \sigma(m)/\sigma(\text{tot}) = 0.27$, is more than two times larger, presumably due to a problem with the time dependence of the decay in Ref. [15]. The total cross section is found to agree within $\pm 1.1\%$ and yields a MACS of $613 \pm 59$, which is still lower than the $741 \pm 30$ mb deduced from the TOF measurement of Ref. [14]. The fact that the present uncertainty is larger than that in the previous measurement of Walter *et al.* [15] is due to the intensity of the $^{80}$Br ground state decay. While Walter *et al.* [15] quote $6.7 \pm 0.4\%$, we use the value of $6.7 \pm 0.6\%$ as given in Ref. [50]. Therefore, the minimum uncertainty (stemming from the intensity only) should be 56 mb for the Walter *et al.* result.

The comparison in Table VII confirms the previously recommended stellar rates of Ref. [10].

### B. $^{81}$Br$(n, \gamma)^{82}$Br cross section

The present MACS value of $235 \pm 9$ mb at 30 keV agrees within the uncertainties with the TOF measurement of Ref. [14], which reported a value of $244 \pm 10$ mb, whereas a severe discrepancy was found compared to the $317 \pm 16$ mb obtained in the previous activation by Walter *et al.* [15]. In this case, the uncertainties of the TOF measurement and of the present activation match perfectly.

### C. $^{85}$Rb$(n, \gamma)^{86}$Rb cross section

As for $^{81}$Br, the present result of $221^{+13}_{-6}$ mb at 30 keV confirms the MACS obtained in the previous TOF measurement [11] of $240 \pm 9$ mb and reveals a severe problem in the older activation [12], which found a 50% higher value. The accuracy of the value obtained in the present activation is very similar to that deduced from the TOF data. However, the energy dependence of this cross section is substantially different in the various evaluations. Therefore, a large uncertainty is obtained for the calculated energy dependence of the MACSs.

### D. $^{87}$Rb$(n, \gamma)^{88}$Rb cross section

Because the neutron-magic isotope $^{87}$Rb acts as an important bottleneck for the *s*-process reaction flow, this cross section has been studied in a series of previous experiments [2,12,13,25]. The respective results for the MACS at $kT = 30$ keV ranged from 11 to 22 mb with uncertainties between 3 and 18%, much smaller than the respective discrepancies. The present value of 15.2 mb has been determined with an uncertainty of 4.3%, in perfect agreement with the TOF measurement of Ref. [13] but two times more accurate. Therefore, the present measurement not only settles the situation for the cross section value but also yields the accuracy required for an improved *s*-process analysis.

In general we find that our results do not agree with the values of previous activation measurements [12] published in 1986. The small changes of the decay properties, which were reported meanwhile, cannot explain the observed discrepancies. In our experiment, systematic uncertainties were considerably reduced by repeated measurements with different sample sizes and chemical compounds, whereas only a single activation was carried out in the rather exploratory work of Ref. [12].

## V. ASTROPHYSICAL IMPLICATIONS

### A. Nuclear input

In combination with a variety of new data the present results have been used for a revision of the branchings at $A = 79$ and 85. In addition to the values listed in Table VII, all other MACSs have been adopted from the KADONIS library, version v0.2 [22], updated with the improved Kr cross sections of Mutti *et al.* [26]. A preliminary experimental cross section has also been reported for $^{78}$Se [27], which appears to be significantly smaller than the semiempirical estimate listed in KADONIS.

Among the stellar $\beta$-decay rates the $\lambda_\beta$ values of the branching points $^{79}$Se and $^{85}$Kr have been treated individually, the first according to the temperature dependence derived from the measurement of Klay and Käppeler [28], and the second by assuming that thermal equilibrium between isomer and ground state in $^{85}$Kr is only reached under carbon shell burning conditions. The $\beta$-decay rates of all other unstable isotopes in the *s*-process path have been adopted from the compilation of Takahashi and Yokoi [7]. At the higher temperatures of carbon shell burning the extrapolated rates of Ref. [2] have been used. Notice that $^{87}$Rb and $^{87}$Sr must be considered as unstable during carbon shell burning.

### B. Stellar models

#### *1. AGB stars*

The stellar model used in this analysis [6] is characterized by the alternate activation of the $^{13}$C$(\alpha, n)^{16}$O and $^{22}$Ne$(\alpha, n)^{25}$Mg reactions in thermally pulsing low mass AGB stars. The first neutron source operates at a comparably low neutron density of about $10^7$ cm$^{-3}$ in the so-called $^{13}$C pocket

during a substantial part of the long shell H burning phase between He shell flashes, where temperatures in the pocket are typically around $0.9 \times 10^8$ K. The $^{13}$C pocket is formed shortly after the He shell flashes by partial mixing of hydrogen from the envelope into a very restricted mass layer of the carbon-rich intershell, thus yielding a high neutron/seed ratio. This reaction provides about 95% of the total neutron exposure.

After the large neutron exposure occurred radiatively in the interpulse period, the pocket is completely engulfed by the subsequent He shell flash. Although the $^{22}$Ne$(\alpha, n)^{25}$Mg reaction is only marginally activated at the temperatures of (2.5 to 3.0)$\times 10^8$ K that are reached at the bottom of the convective He shell flashes, a small neutron burst but of comparably high peak neutron densities of $\approx 10^{**}$ 10 cm$^{**}$ $-3^{**}$ occurs in that stage. Despite the fact that the contribution of the $^{22}$Ne$(\alpha, n)^{25}$Mg source to the total neutron exposure is limited to about 5% because of the much shorter duration of this phase, this suffices to modify the abundance patterns of the *s*-process branchings with respect to the $^{13}$C pocket signature significantly.

The model used for obtaining the solar *s*-process contribution of the main component from low mass AGB stars was following the prescription of Arlandini *et al.* [8], i.e., using the average of models for 1.5 and 3 $M_\odot$ and half solar metallicity.

#### 2. *Massive stars*

The weak *s* process, which takes place during the presupernova evolution of massive stars with $M \geqslant 8$ $M_\odot$, is responsible for most of the *s* abundances between the iron peak and strontium as discussed, e.g., in Ref. [2]. Neutrons are mainly produced by the $^{22}$Ne$(\alpha, n)^{25}$Mg reaction during convective core He burning and the subsequent convective shell C burning.

During the core He burning phase, the *s* process is considered as a secondary nucleosynthesis process, because the $^{22}$Ne in this phase is produced from the $^{14}$N resulting from the conversion of the initial CNO abundances during core H burning and is, therefore, determined by the initial stellar metallicity [29–31]. Soon after the start of convective core He burning, $^{14}$N is fully converted to $^{18}$O via $^{14}$N$(\alpha, \gamma)^{18}$F$(\beta^+\nu)^{18}$O. Later on, when $^4$He has been depleted to about 10% in mass fraction and the central temperature has increased to $T_8 \approx 2.5$, $\alpha$ captures on $^{18}$O lead to $^{22}$Ne, making the $^{22}$Ne$(\alpha, n)^{25}$Mg reaction an efficient neutron source in the last phases of core He burning, close to He exhaustion, when central temperatures of $T_8 = 3$–3.5 are reached [31].

The major parts of the products of core He burning are subsequently exposed to a second neutron irradiation during the convective shell C burning phase, when temperatures of $\sim 10^9$ K and densities of $\sim 10^5$ g/cm$^3$ are reached at the bottom of the shell. In the 25 $M_\odot$ model used for the present discussion, the outer convective shell extends during C burning from about 2 $M_\odot$ to about 6 $M_\odot$, close to the maximum extension of the previous convective He burning core. Carbon burns via the reaction channels $^{12}$C$(^{12}$C, $\alpha)^{20}$Ne and $^{12}$C$(^{12}$C, $p)^{23}$Na, thus providing the $\alpha$ particles for $^{22}$Ne$(\alpha, n)^{25}$Mg reactions on the surviving $^{22}$Ne from the former He core. The contributions of other $(\alpha, n)$ reactions to the neutron balance, e.g., on $^{18}$O, $^{25}$Mg, and $^{26}$Mg, are negligible. $^{13}$C$(\alpha, n)^{16}$O and $^{17}$O$(\alpha, n)^{21}$Ne recycle neutrons previously captured by $^{12}$C and $^{16}$O, respectively.

Nucleosynthesis of the light isotopes during C burning was discussed already in Ref. [32], whereas a detailed *s*-process nucleosynthesis during this phase was first considered in 1991 [1]. This contribution to the weak *s* process is characterized by a short time scale of about 1 yr and high neutron densities of $10^{11}$ to $10^{12}$ cm$^{-3}$. These first results were later confirmed by full network calculations for stellar evolution up to the supernova explosion [33–37]. For a 25 $M_\odot$ star, the abundances in the inner zone up to $\sim$3.5 $M_\odot$ are destroyed or strongly modified by photodisintegration in the supernova explosion, but the *s*-process material in the outer layers of the convective C burning shell is ejected substantially unchanged [34,36].

The present calculations were performed with a stellar model for a 25 $M_\odot$ star and solar metallicity [38]. An improved time-dependent treatment was used for C shell burning [33,39], which leads to a late increase of the neutron density during the last day of this phase.

### C. The branchings at $^{79}$Se and $^{85}$Kr

Because *s*-process branchings carry the signatures of the high neutron densities and temperatures reached in the He shell flash, they represent sensitive tests of stellar models for the AGB phase. A general survey of the *s*-process abundance patterns produced in AGB stars by Arlandini *et al.* [8] has been recently updated [40] using the significantly improved nuclear input described before. In this context, the present cross section results are important for the description of the branchings at $^{79}$Se and $^{85}$Kr.

Figure 1 illustrates the *s*-process path between Se and Sr. While the branching at $^{79}$Se is mostly determined by the weak component, the one at $^{85}$Kr is about equally influenced by the main component. In this case, the 4.48 h isomer in $^{85}$Kr and the effect of the magic neutron number $N = 50$ also have a strong impact on the resulting abundance pattern.

The results obtained with the present MACS values of the Br and Rb isotopes are summarized in columns 2 and 5 of Table VIII. A comprehensive discussion of the underlying stellar model calculations for AGB stars and for massive stars is given in Refs. [41] and [38], respectively. The main consequences for the $^{79}$Se and $^{85}$Kr branchings can already be sketched from the comparison given in Table VIII. The abundance distributions from the weak *s* process are normalized to 83% of the solar $^{70}$Ge abundance, assuming that 7% are coming from the main component [8] and 10% from the *p* process [42]. This normalization has been applied to the values taken from Refs. [2] and [37] as well.

#### 1. $^{79}$Se *branching*

The $^{79}$Se branching is characterized by the pronounced temperature dependence of the decay rate of $^{79}$Se [28]. This rate is the only known case where the temperature dependence could be based on an experimental value for the lifetime of

TABLE VIII. Abundance components due to the weak and main $s$ processes obtained with present data and updated models (as fraction of solar values [48]).

| Isotope | Low mass stars | | Massive stars (Core He + Shell C) | | | Total $s$ abundance This Work[e] |
|---|---|---|---|---|---|---|
| | Arlandini *et al.*[a] | This work | Raiteri *et al.*[b] | The *et al.*[c] | This work[d] | |
| $^{78}$Se | 0.11 | 0.088 | 0.48 | ... | 0.82 | 0.91 |
| $^{80}$Se | 0.088 | 0.092 | 0.19 | 0.20 | 0.30 | 0.39 |
| $^{82}$Se | 0.001 | 0.001 | ... | ... | 0.06 | 0.06 |
| $^{79}$Br | 0.087 | 0.077 | 0.38 | ... | 0.55 | 0.62 |
| $^{81}$Br | 0.093 | 0.097 | 0.25 | ... | 0.21 | 0.31 |
| $^{80}$Kr | 0.12 | 0.109 | 1.11 | 0.28 | 0.21 | 0.32 |
| $^{82}$Kr | 0.37 | 0.299 | 0.69 | 0.52 | 0.57 | 0.87 |
| $^{83}$Kr | 0.13 | 0.111 | 0.25 | ... | 0.33 | 0.44 |
| $^{84}$Kr | 0.14 | 0.142 | 0.18 | ... | 0.24 | 0.38 |
| $^{86}$Kr | 0.27 | 0.182 | 0.17 | 0.20 | 0.22 | 0.40 |
| $^{85}$Rb | 0.16 | 0.170 | 0.25 | ... | 0.24 | 0.41 |
| $^{87}$Rb | 0.35 | 0.240 | 0.18 | 0.26 | 0.46 | 0.70 |
| $^{86}$Sr | 0.47 | 0.564 | 0.31 | 0.16 | 0.23 | 0.79 |
| $^{87}$Sr | 0.50 | 0.567 | 0.21 | 0.16 | 0.12 | 0.69 |
| $^{88}$Sr | 0.92 | 1.021 | 0.09 | 0.11 | 0.07 | 1.09 |
| $^{89}$Y | 0.92 | 0.987 | 0.06 | ... | 0.07 | 1.06 |
| $^{90}$Zr | 0.72 | 0.727 | 0.03 | ... | 0.03 | 0.76 |

[a]Reference [8].
[b]Reference [2], normalized to 83% of solar 70 Ge abundance (see text).
[c]Reference [37], case N, normalized to 83% of solar 70 Ge abundance (see text).
[d]Model with rising temperature at the end of carbon shell burning [38].
[e]Sum of columns 3 and 6.

the thermally populated excited state, which is responsible for the enhancement. Therefore, the $^{79}$Se branching represents a unique $s$-process thermometer. An improvement of the stellar $(n, \gamma)$ cross sections of $^{79}$Br and $^{81}$Br adds significantly to the quantitative description of the further reaction flow toward the $s$-only isotopes $^{80}$Kr and $^{82}$Kr.

The abundance contributions from the main component, i.e., from thermally pulsing low mass AGB stars, are compared in columns 2 and 3 of Table VIII. An obvious difference from of Ref. [8] is the lower overall $s$ abundances, e.g., indicated by the unbranched isotopes $^{78}$Se and $^{82}$Kr. However, the $^{81}$Br abundance deviates from this trend because the present cross section is 30% lower than the previous value [10], resulting in a correspondingly higher $s$-process yield.

The situation in massive stars is complicated by the fact that the model predictions seem to differ mostly because of the adopted neutron densities as indicated by the $^{80}$Kr abundances [2,37]. Because of the very high peak neutron densities reached in C shell burning, it was found that the final $^{80}$Kr abundance depends strongly on the freeze-out phase. This led to a significant overproduction of $^{80}$Kr in models assuming a constant temperature during C shell burning, similar to the value given in Ref. [2]. Therefore, an improved time-dependent treatment of C shell burning, which leads to a late increase of the neutron density [33,39], has been considered in the present calculations. With this approach the overproduction of $^{80}$Kr could be avoided, but our calculations clearly show that the $^{80}$Kr abundance is strongly affected by the neutron density history in the last C shell phase, which may be different considering different stellar model results (e.g., Refs. [33,37]). Moreover, according to Ref. [36], $^{80}$Kr may have a strong explosive contribution that is uncertain.

With respect to the total $s$ production obtained in this work (columns 3 and 6), one finds that the unbranched $s$-only isotope $^{82}$Kr is well reproduced within the present uncertainties, which means that the $s$-process efficiency is correctly described.

### 2. $^{85}$Kr *branching*

For the subsequent branching at $^{85}$Kr, which defines the $s$-process components of the Rb and Sr isotopes, thermal effects are of minor importance. This is illustrated by means of the level scheme in Fig. 5. Apart from the ground state of $^{85}$Kr ($t_{1/2} = 10.76$ yr) and the 4.48 h isomer at 305 keV, there are no other states in $^{85}$Kr below 1100 keV excitation energy. The isomer is strongly populated by $(n, \gamma)$ reactions on $^{84}$Kr and decays predominantly via $\beta$ decay (86%). Thermal couplings between the two states through higher lying mediating levels, which could lead to an enhancement of the decay rate, are practically excluded at $s$-process temperatures [7,43], except under the conditions prevailing during carbon shell burning in massive stars ($kT \sim 90$ keV) [2]. This means that the strength of the $^{85}$Kr branching is essentially characterized by the neutron density alone in most of the $s$-process sites.

This sensitivity is strongly enhanced by the fact that the neutron capture and $\beta$ decay parts of the branching are determined by isotopes with very different $(n, \gamma)$ cross sections. The neutron capture branch is producing the neutron-magic

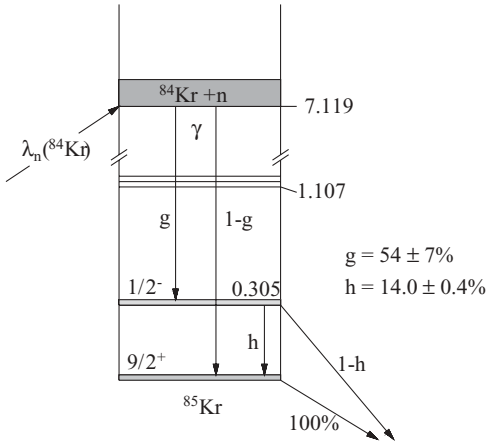


FIG. 5. Schematics of the $^{85}$Kr branching. The feeding probability $g$ was obtained from the ratio of the partial cross section to the isomer [10] and the total $(n, \gamma)$ cross section of $^{84}$Kr [26], and the decay parameter $h$ is from Ref. [53].

isotopes $^{86}$Kr, $^{87}$Rb, and $^{88}$Sr. Because of their very small cross sections, the abundances of these isotopes are enhanced with respect to $^{85}$Rb and $^{86,87}$Sr, which are fed by the $\beta$-decay branch. This effect of the neutron density is reflected in solar system material and more specifically in presolar dust grains [44]. The signature of the neutron density affects even the elemental Rb and Sr ratio and was, therefore, used to estimate the neutron density by spectroscopy of stars with different metallicity and different *s*-process enrichments [45–47]. This aspect of the Sr/Rb ratio also plays an important role in GCE studies [9].

Because the cross sections for $^{85}$Rb and $^{87}$Rb are practically confirming the previous values [10]—apart from the improved accuracy—for AGB stars, the large differences compared to the abundance pattern of Arlandini *et al.* [8] point to a lower neutron density, because the neutron capture branch via $^{86}$Kr and $^{87}$Rb is considerably weaker in the present data, whereas the $^{86,87}$Sr abundances are enhanced. Moreover, it is interesting to note that the *s*-dominated abundances of the unbranched isotopes $^{88}$Sr and $^{89}$Y are enhanced with respect to Ref. [8], in opposition to the observations in the Br/Kr region. This effect indicates a higher *s*-process efficiency, probably due to a higher neutron/seed ratio in the $^{13}$C pocket.

As noted before, *s*-process calculations in massive stars are hampered by the wider range of neutron densities. In the present approach that assumes an increase in temperature at the end of C shell burning, the abundance pattern is shaped by the concomitant increase in neutron density. In particular, in the C shell $^{85}$Kr is efficiently produced and accumulated, according to its neutron capture cross section that is theoretical and uncertain by a factor of two at least. At the end of the neutron flow, all the $^{85}$Kr left will feed $^{85}$Rb by radiogenic decay. This means that the final $^{85}$Rb is strongly affected by the $^{85}$Kr cross section. For example, in the C shell model used in the present calculations the final $^{85}$Kr is about five times more abundant than $^{85}$Rb. Considering that $^{85}$Rb is more than 70% of the solar Rb and that the *s* process in massive stars provides a significant contribution to the solar $^{85}$Rb, we stress that an experimental evaluation of the $^{85}$Kr neutron capture cross section is very important for Rb nucleosynthesis.

### D. Solar *s* abundances

As far as the total *s* abundances are concerned, the solar distribution appears to be rather well reproduced by the sum of the weak and main components in column 7 of Table VIII, indicating that the *s*-process efficiency is properly described on average. An important exception is the very low abundance of the important *s*-only isotope $^{80}$Kr.

As discussed before, the production of $^{80}$Kr in massive stars is affected by the treatment of the shell C burning and by explosive nucleosynthesis. As shown by the comparison in Table VIII, the *s* abundances obtained are systematically higher than those reported previously in Refs. [2] and [37]. These uncertainties may be responsible for the difficulties in reproducing the branchings at $^{79}$Se and $^{85}$Kr. In the light of these results, where stellar model uncertainties are combined with nuclear uncertainties related to the unstable $^{79}$Se, the underproduction of $^{80}$Kr finds a reasonable explanation. The mild overproduction of the *s*-dominated isotopes $^{88}$Sr and $^{89}$Y is practically within the uncertainties of the solar abundances and, therefore, less disturbing.

Stellar spectroscopy can provide important constraints for the model predictions of the Rb/Sr ratio in AGB stars. In general, the Rb/Sr ratio represents a signature of the *s*-process neutron density provided by the $^{22}$Ne$(\alpha, n)^{25}$Mg source. At high neutron density, $^{87}$Rb is fed through the neutron channels of the branchings at $^{85}$Kr and $^{86}$Rb. On the contrary, low neutron densities favor the $\beta$-decay channels of these branchings. Consequently, this is connected with a high or low Rb abundance as the consequence of the small and large MACSs of $^{87}$Rb and $^{85}$Rb, respectively. With the Rb cross sections reported here, the accuracy of the elemental *s* abundance of Rb could be improved by a factor of two. This implies a slightly lower Rb/Sr ratio of $0.065 \pm 0.009$ compared to the previous value of $0.076 \pm 0.011$ [8]. Because the observed yttrium abundance might be a more reliable indicator for the unbranched reaction flow [46], the Rb/Y ratios obtained with the old and new cross sections have been determined as well, yielding Rb/Y ratios of $0.33 \pm 0.04$ and $0.31 \pm 0.03$, respectively.

The results for low mass stars in Table VIII can, in principle, be used to derive the corresponding envelope abundances for comparison with the [Rb/Y] and [Rb/Sr] values obtained from abundance observations in AGB stars, e.g., with those shown in Fig. 3 of Ref. [46], provided that these stars are intrinsic AGB stars. However, the present cross section values at thermal energies around $kT = 25$ keV—where the final abundances in low mass AGB stars are formed—are rather similar by number to those given in Ref. [10], which were used in previous studies. Therefore, the present values confirm the previous attempts to constrain the neutron density through observations of the elemental Rb/Sr and Rb/Y abundance ratios in thermally pulsing low mass AGB stars within the observational uncertainties [45–47].

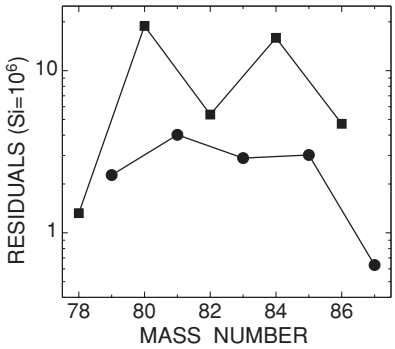


FIG. 6. Abundance residuals obtained as the difference between solar values and the total $s$-process abundances listed in column 7 of Table VIII, $N_\odot - N_s$. The structure in the abundance patterns of the even (squares) isotopes differs from the characteristic smoothness of the $r$-process residuals in the mass region $A \geqslant 100$ [8].

For completeness, the "$r$" residuals obtained as the difference between the solar abundance values [48] and the total $s$ abundances listed in column 7 of Table VIII, $N_\odot - N_s$, are plotted in Fig. 6. It is interesting to note the structure in the abundance patterns of the even isotopes, which is in contrast to the smoothness of the $r$-process residuals in the mass region $A \geqslant 100$ [8]. A serious discussion of this point would require more accurate cross sections for Se isotopes and a comprehensive study of GCE effects. Both aspects are, however, clearly beyond the scope of this article.

## VI. CONCLUSIONS

The stellar $(n, \gamma)$ cross sections of $^{79,81}$Br and $^{85,87}$Rb have been determined by a series of activation measurements, using the $^{7}$Li$(p, n)^{7}$Be reaction for producing a quasistellar neutron spectrum at a thermal energy of $kT = 25$ keV. Systematic uncertainties have been derived from repeated runs, which were performed under different experimental conditions.

The consequences of the new data for the $s$-process production by the weak $s$ components and the main $s$ components have been discussed with updated nuclear input and by invoking current models for massive stars and for thermally pulsing low mass AGB stars. From the study of the abundance patterns in the mass region of the $^{79}$Sr and $^{85}$Kr branchings, uncertainties have been found to mostly result from the neutron density history in the convective C shell in massive stars [37,38] and from the neutron capture cross sections of unstable isotopes like $^{79}$Se, $^{85}$Kr, and $^{86}$Rb.

It has been found that the improved Rb abundances obtained via the present cross section data do not alter the findings of previous attempts to constrain the neutron density through observations of the elemental Rb/Sr and Rb/Y abundance ratios in thermally pulsing low mass AGB stars [45–47].

## ACKNOWLEDGMENTS

We are thankful to D. Roller, E.-P. Knaetsch, and W. Seith for their support during the measurements. M.P., S.B., and R.G. acknowledge support by the Italian MIUR-PRIN06 Project 2006022731_005. M.P. also acknowledges the Marie Curie International Reintegration Grant within the 6th European Community Framework Programme, Grant MIRG-CT-2006-046520, and NSF Grant PHY 02-16783 (Joint Institute for Nuclear Astrophysics).

[1] C. Raiteri, M. Busso, R. Gallino, and G. Picchio, Astrophys. J. **371**, 665 (1991).
[2] C. Raiteri *et al.*, Astrophys. J. **419**, 207 (1993).
[3] T. Rauscher, A. Heger, R. Hoffman, and S. Woosley, Astrophys. J. **576**, 323 (2002).
[4] H. Nassar *et al.*, Phys. Rev. Lett. **94**, 092504 (2005).
[5] O. Straniero *et al.*, Astrophys. J. **440**, L85 (1995).
[6] R. Gallino *et al.*, Astrophys. J. **497**, 388 (1998).
[7] K. Takahashi and K. Yokoi, At. Data Nucl. Data Tables **36**, 375 (1987).
[8] C. Arlandini *et al.*, Astrophys. J. **525**, 886 (1999).
[9] C. Travaglio *et al.*, Astrophys. J. **601**, 864 (2004).
[10] Z. Bao *et al.*, At. Data Nucl. Data Tables **76**, 70 (2000).
[11] H. Beer and R. Macklin, Astrophys. J. **339**, 962 (1989).
[12] G. Walter, H. Beer, F. Käppeler, and R.-D. Penzhorn, Astron. Astrophys. **155**, 247 (1986).
[13] S. Jaag and F. Käppeler, Phys. Rev. C **53**, 2474 (1996).
[14] R. Macklin, Nucl. Sci. Eng. **99**, 133 (1988).
[15] G. Walter *et al.*, Astron. Astrophys. **167**, 186 (1986).
[16] H. Beer and F. Käppeler, Phys. Rev. C **21**, 534 (1980).
[17] W. Ratynski and F. Käppeler, Phys. Rev. C **37**, 595 (1988).
[18] N. Patronis *et al.*, Phys. Rev. C **69**, 025803 (2004).
[19] S. O'Brien *et al.*, Phys. Rev. C **68**, 035801 (2003).
[20] U. Ratzel *et al.*, Phys. Rev. C **70**, 065803 (2004).
[21] R. Reifarth and F. Käppeler, Phys. Rev. C **66**, 054605 (2002).
[22] I. Dillmann *et al.*, in *Capture Gamma-Ray Spectroscopy and Related Topics*, *AIP Conference Series 819*, edited by A. Woehr and A. Aprahamian (AIP, New York, 2005), p. 123, http://www.kadonis.org.
[23] B. Singh, Nucl. Data Sheets **105**, 223 (2005).
[24] G. Walter, Report KfK 3706, Forschungszentrum Karlsruhe, 1984.
[25] H. Beer and R. Macklin, Astrophys. J. **331**, 1047 (1988).
[26] P. Mutti *et al.*, in *Nuclear Data for Science and Technology*, *AIP Conference Series 769*, edited by R. Haight, M. Chadwick, T. Kawano, and P. Talou (AIP, New York, 2005), pp. 1327–1330.
[27] I. Dillmann *et al.*, in *International Symposium on Nuclear Astrophysics, Nuclei in the Cosmos—IX*, *PoS—Proceedings of Science, ISSN 18248039*, edited by A. Mengoni *et al.* (SISSA, Trieste, 2006), article 089, http://pos.sissa.it.
[28] N. Klay and F. Käppeler, Phys. Rev. C **38**, 295 (1988).
[29] S. Lamb, W. Howard, J. Truran, and I. Iben, Astrophys. J. **217**, 213 (1977).
[30] N. Prantzos, M. Arnould, and J.-P. Arcoragi, Astrophys. J. **315**, 209 (1987).
[31] C. Raiteri *et al.*, Astrophys. J. **367**, 228 (1991).
[32] W. Arnett and J. Truran, Astrophys. J. **157**, 339 (1969).
[33] M. Limongi, O. Straniero, and A. Chieffi, Astrophys. J. Suppl. **129**, 625 (2000).

[34] M. Limongi, technical report, http://www.mporzio.astro.it/∼limongi/ (unpublished).
[35] S. Woosley, A. Heger, and T. Weaver, Rev. Mod. Phys. **74**, 1015 (2002).
[36] A. Heger, technical report, http://www.ucolick.org/∼alex/ (unpublished).
[37] L. The, M. El Eid, and B. Meyer, Astrophys. J. **655**, 1058 (2007).
[38] M. Pignatari *et al*. (in preparation).
[39] W. Arnett and J. Wefel, Astrophys. J. **224**, L139 (1978).
[40] S. Bisterzo *et al*., in *International Symposium on Nuclear Astrophysics, Nuclei in the Cosmos—IX*, *PoS—Proceedings of Science, ISSN 18248039*, edited by A. Mengoni *et al*. (SISSA, Trieste, 2006), article 077, http://pos.sissa.it.
[41] S. Bisterzo, Ph.D. thesis, University of Torino, Italy, 2007.
[42] F. Käppeler, H. Beer, and K. Wisshak, Rep. Prog. Phys. **52**, 945 (1989).
[43] R. Ward, Astrophys. J. **216**, 540 (1977).
[44] R. Lewis, S. Amari, and E. Anders, Geochim. Cosmochim. Acta **58**, 471 (1994).
[45] J. Tomkin and D. Lambert, Astrophys. J. **523**, 234 (1999).
[46] C. Abia *et al*., Astrophys. J. **559**, 1117 (2001).
[47] C. Abia *et al*., Astrophys. J. **579**, 817 (2002).
[48] E. Anders and N. Grevesse, Geochim. Cosmochim. Acta **53**, 197 (1989).
[49] J. Tuli, Nucl. Data Sheets **98**, 209 (2003).
[50] B. Singh, Nucl. Data Sheets **94**, 1 (2001).
[51] G. Mukherjee and A. Sonzogni, Nucl. Data Sheets **105**, 419 (2005).
[52] Z. Chunmei, Nucl. Data Sheets **95**, 59 (2002).
[53] R. Firestone, in *Table of Isotopes*, edited by V. Shirley (Wiley, New York, 1996).